Published in final edited form as:
Cell Rep. 2014 October 23; 9(2): 674–687. doi:10.1016/j.celrep.2014.09.019.

ESCRT-II/Vps25 constrains digit number by endosome-mediated selective modulation of FGF-SHH signaling

Karen Handschuh[1,11], **Jennifer Feenstra**[1,11], **Matthew Koss**[1,11], **Elisabetta Ferretti**[1], **Maurizio Risolino**[1], **Rediet Zewdu**[1], **Michelle A. Sahai**[2], **Jean-Denis Bénazet**[1], **Xiao P. Peng**[1], **Michael J. Depew**[3,4], **Laura Quintana**[1,5], **James Sharpe**[5,6], **Baolin Wang**[7], **Heather Alcorn**[8], **Roberta Rivi**[8], **Stephen Butcher**[9], **J Robert Manak**[9], **Thomas Vaccari**[10], **Harel Weinstein**[2], **Kathryn V. Anderson**[8], **Elizabeth Lacy**[8], and **Licia Selleri**[1,*]

[1]Department of Cell and Developmental Biology, Weill Cornell Medical College, New York, NY 10065, USA

[2]Department of Physiology and Biophysics, Weill Cornell Medical College, New York, NY 10065, USA

[3]Department of Craniofacial Development, King's College London, Guy's Hospital, London Bridge, London SE1 9RT, UK

[4]Department of Othopaedic Surgery, UCSF, San Francisco, CA 94110, USA

[5]Centre for Genomic Regulation (CRG), and Universitat Pompeu Fabra (UPF), 08003 Barcelona, Spain

[6]Institucio Catalana de Recerca i Estudis Avancats (ICREA), 08010 Barcelona, Spain

[7]Department of Genetic Medicine, Weill Cornell Medical College, New York, NY 10065, USA

[8]Developmental Biology Program, Sloan-Kettering Institute, New York, NY 10065, USA

[*]Correspondence: Licia Selleri, lis2008@med.cornell.edu.
[11]These authors contributed equally to this work

Author Contributions

K.H. and J.F. conducted high-resolution mapping; identified *Vps25* mutation; completed genetic complementation; performed skeletal preparations, ISH, IF, TEM, IP and WB experiments; did the genetic rescue experiments; and assisted L.S. in manuscript writing. M.K. participated in the ENU screen; conducted high-resolution mapping; cloned tagged Vps20 and Vps25 WT and mutant expression constructs; and performed qRT-PCR for *Vps25* expression levels. E.F. participated in the ENU screen; performed skeletal preparations; and conducted initial high-resolution mapping. M.R. performed qRT-PCR for *Shh*, *Patched1*, *Gli1* in limb buds and MEFs; did statistical analyses; and contributed to manuscript writing. R.Z. established that the Vps25 mutation is hypomorphic by WB; generated MEF lines; and contributed to manuscript writing. M.A.S. and H.W. conducted 3D modeling of WT and $Vps25^{ENU}$ proteins and contributed to manuscript writing. J-D. B. provided qRT-PCR primers for *Shh*, *Patched1*, and *Gli1* and assisted the interpretation of limb ISH data. X.P.P. identified involvement of pSTAT3 as second messenger of FGF hyperactivation. M.D. analyzed skeletal preparations of all ENU-mutagenized lines. L.Q. and J.S. performed OPT and 3D analysis of limbs for Vps25 mutant line. B.W. provided a Gli3 antibody. H.A. assisted in deep sequencing. R.R. conducted embryo dissections throughout ENU screen. S.B. and J.R.M. conducted microarray experiments and analyses for gene finding. T.V. performed analyses of MVB and lysosomal diameters and provided suggestions to explore abnormal ESCRT function. K.V.A. initiated the ENU screen; gave input for high-resolution mapping and analysis of the SHH pathway. E.L. participated in the ENU screen and in analysis and interpretation of all data. L.S. conducted embryo dissections throughout ENU screen; designed project; and wrote the manuscript.

[9]Departments of Biology and Pediatrics, University of Iowa, Iowa City, IA 52242, USA

[10]IFOM - FIRC Institute of Molecular Oncology, 20139 Milan, Italy

Summary

Sorting and degradation of receptors and associated signaling molecules maintain homeostasis of conserved signaling pathways during cell specification and tissue development. Yet, whether machineries that sort signaling proteins act preferentially on different receptors and ligands in different contexts remains mysterious. Here we show that Vacuolar protein sorting 25, Vps25, a component of ESCRT-II (Endosomal Sorting Complex Required for Transport II), directs preferential endosome-mediated modulation of FGF signaling in limbs. By ENU-induced mutagenesis we isolated a polydactylous mouse line carrying a hypomorphic mutation of *Vps25* (*Vps25*^{ENU}). Unlike *Vps25*-null embryos we generated, *Vps25*$^{ENU/ENU}$ mutants survive until late gestation. Their limbs display FGF signaling enhancement and consequent hyper-activation of the FGF-SHH feedback loop causing polydactyly, whereas WNT and BMP signaling remain unperturbed. Notably, *Vps25*$^{ENU/ENU}$ Mouse Embryonic Fibroblasts exhibit aberrant FGFR trafficking and degradation; however SHH signaling is unperturbed. These studies establish that the ESCRT-II machinery selectively limits FGF signaling in vertebrate skeletal patterning.

Introduction

The complexity of development is dependent upon signal transduction pathways, which are critical for cell specification, tissue patterning, organ morphogenesis and growth. Notably, the embryo constructs markedly different structures by using the same signaling pathways (Wolpert, 1994). The developing vertebrate limb can serve as a tractable model to analyze mechanisms of cell signaling (Zeller, 2010).

In vertebrates, limb development is controlled by two signaling centers, the apical ectodermal ridge (AER) at the distal bud and the zone of polarizing activity (ZPA) in the posterior mesenchyme (Zeller, 2010). Both centers produce instructive signals that direct anterior-posterior (AP) and proximal-distal (PD) limb axis formation. The AER produces multiple fibroblast growth factors (FGF8, FGF4, FGF9, FGF17), while the ZPA produces Sonic Hedgehog (SHH) (Tabin and Wolpert, 2007). Throughout limb development, the AER and ZPA are interlinked by a feedback signaling loop, which is also influenced by other signaling molecules and transcription factors (Tabin and Wolpert, 2007; Zakany and Duboule, 2007; Zeller et al., 2009). Genetic mutations that perturb the FGF-SHH loop lead to alterations of the highly conserved pentadactyl pattern (Biesecker, 2011). Therefore, how cells maintain signaling homeostasis is critical for the establishment of digit number and identity.

Homeostasis of signaling proteins is maintained through sorting and degradation via endosome-mediated vesicular trafficking (MacGurn et al., 2012). Mutations of ESCRT (Endosomal Sorting Complex Required for Transport) machinery components compromise their ability to degrade conserved signaling proteins in multiple organisms (Henne et al., 2011 & 2013). Indeed, ESCRT LOF models display perturbations of signaling (Rusten et al., 2012). However, early lethality of mutants with complete LOF of ESCRT components

(Rusten et al., 2012) and the absence of conditional or hypomorphic mutations has prevented understanding how ESCRT members contribute to shaping organismal forms. Furthermore, whether constitutively expressed multi-component ESCRT machineries act on different receptors and associated signaling proteins in a specialized or preferential manner in different contexts of the developing embryo remains poorly understood.

Here, identification of a hypomorphic mutation in the ESCRT-II complex in a polydactylous mouse line isolated by a N-ethyl-N-nitrosourea (ENU) mutagenesis screen (Anderson and Ingham, 2003; Stottmann and Beier, 2010) allowed deconstruction of the mechanisms by which specific ESCRT components execute patterning and morphogenetic processes. This unique mouse model with a partially functional ESCRT-II allele afforded testing of the hypothesis that ubiquitously expressed ESCRT machineries act on different receptors and associated signaling proteins in a preferential manner in different embryonic contexts, such as the developing limb bud.

Results

Isolation of *04-014* mouse line with polydactyly through a N-ethyl-N-nitrosourea mutagenesis screen and identification of the ENU-induced mutation in the *Vps25* gene

By a N-ethyl-N-nitrosourea (ENU) mutagenesis screen, we isolated mouse line *04-014* based on recessive hindlimb polydactyly with variable expressivity (Figure 1A–1D). We located the mutation within the murine ortholog of yeast Vacuolar protein sorting 25, *Vps25* (also known as *EAP20*), encoding a subunit of the ESCRT-II complex (Babst et al., 2002b; Slater and Bishop, 2006) essential for endosomal protein trafficking (Henne et al., 2011; MacGurn et al., 2012; Rusten et al., 2012) (Figures 1E, Table S1). Identified by sequencing of candidate gene cDNA, and confirmed by deep sequencing (Arnold et al., 2011) of the narrowest genomic interval linked to the mutation (Table S1), a G-to-A transition in *Vps25* third intron generated an mRNA splice variant containing an in-frame 27-nucleotide insertion encoding 9 additional neutral amino acids (Figures 1E–1G, S1A, Table S2). Hereafter, the ENU-induced allele will be designated $Vps25^{ENU}$ and the recessive homozygous mutant embryos $Vps25^{ENU/ENU}$.

ENU-induced mutation of ESCRT-II/*Vps25* results in a partially functional hypomorphic allele, while LOF causes early gestational lethality

To characterize effects of the ENU-induced mutation on *Vps25* transcription, qRT-PCR detected the *Vps25* splice variant as well as wild-type (WT) mRNA in the mutants. However, in mutant embryos at various gestational days, both mRNA species and their encoded proteins were significantly less abundant than WT *Vps25* in WT littermates (Figures 1H,1I, S1B). Thus, the ENU-induced allele is hypomorphic affording analysis of how ESCRT-II/Vps25 execute patterning and morphogenesis in vertebrate development.

To elucidate the requirements for *Vps25* during development, we compared the activity of $Vps25^{ENU}$ to a *Vps25* global LOF allele ($Vps25^{LacZ}$) we generated by replacing *Vps25* with a LacZ/Neo cassette (www.komp.org). At E8.5 no $Vps25^{LacZ/LacZ}$ embryos were recovered, only empty deciduae, defining the *Vps25* LOF allele as more deleterious than $Vps25^{ENU}$

(Figure S1C). Thus, similar to LOF of other mouse ESCRT components (Komada and Soriano, 1999; Lee et al., 2007; Ruland et al., 2001; Shim et al., 2006; Yamada et al., 2002), global *Vps25* LOF causes early lethality *in utero*. Consistent with early lethality, RT-PCR and X-gal staining of $Vps25^{LacZ/+}$ embryos corroborated widespread *Vps25* expression, including in limbs, from E9.5-E13.5 (Figures 1J–1M, S1D–S1J). Absence of complementation between $Vps25^{LacZ}$ and $Vps25^{ENU}$ in trans-heterozygous $Vps25^{LacZ/ENU}$ embryos confirmed the G-to-A transition in *Vps25* intron 3 as the causative mutation (Figure 1N–1Q, Table S3). As predicted for a hypomorphic allele, $Vps25^{ENU/ENU}$ embryos survived until E15.5–16.5 on a mixed genetic background (Figure 1Q), whereas $Vps25^{LacZ/ENU}$ embryos exhibited developmental delay and hemorrhaging as early as E9.5 (Figure 1P).

ENU-induced mutation of ESCRT-II/*Vps25* causes fully penetrant polydactyly

Skeletal preparations and Optical Projection Tomography (Sharpe et al., 2002) (OPT) revealed fully penetrant hindlimb polydactyly (Figures 2A–2D, Movie S1–S2), while in mutant forelimbs polydactyly was less severe and not fully penetrant (Figure S2A–S2F′, Movie S3–S4). Compared to WT, the mutant scapular blade was thinner with a central hole (Figure S2G, S2G′). Mutant limbs also exhibited shorter and thicker skeletal elements (Figures 2A,2B, S2H–S2L′).

To uncover the cellular behaviors underlying the polydactyly, we examined proliferation (Koss et al., 2012) and apoptosis (Ferretti et al., 2011) in WT and $Vps25^{ENU/ENU}$ limbs (Figure 2E–2L). E12.5 WT hindlimb showed a highly proliferative mesenchyme and a quiescent anterior AER (Figure 2E,2G). In contrast, hindlimb anterior AER of $Vps25^{ENU/ENU}$ littermates appeared strikingly proliferative (Figure 2F,2H). Additionally, unlike WT (Figure 2I,2K), $Vps25^{ENU/ENU}$ anterior hindlimb contained no detectable cell death (Figures 2J,2L, S2U–S2X). We observed similar, albeit less pronounced, proliferation and apoptosis defects in $Vps25^{ENU/ENU}$ forelimbs (Figure S2M–S2T). *Msx2*, a marker of apoptotic cells (Lallemand et al., 2009), was expressed in the inter-digital spaces and around digit 1 of E13.5 WT hindlimb; however, $Vps25^{ENU/ENU}$ hindlimb bud lacked *Msx2* in the domain where polydactyly arises (Figure 2M,2N). Lastly, *Sox9* expression (Mariani and Martin, 2003) appeared diffuse in E13.5 $Vps25^{ENU/ENU}$ hindlimb anterior mesenchyme, suggesting multiple digit condensations (Figure 2O,2P). These results implicate perturbations of proliferation and cell death in $Vps25^{ENU/ENU}$ anterior limb domains as the underlying causes of polydactyly or synpolydactlyly.

$Vps25^{ENU/ENU}$ early limb buds exhibit specific enhancement of the FGF-SHH cross-regulatory loop underlying polydactyly, while WNT and BMP signaling are unperturbed

To assess whether *Vps25* mutation induced ESCRT-II-dependent perturbation of signaling molecules critical for limb patterning, we analyzed their expression by whole-mount *in situ* hybridization (Figure 3). We examined the signaling loop between AER-FGF and ZPA-SHH. SHH activation requires not only FGFs, but also Hand2 and 5′ HoxD transcription factors (Zakany and Duboule, 2007). Notably, perturbations of 5′ *Hox* genes on *Gli3*-null background (Lopez-Rios et al., 2012) yield more severe polydactyly than LOF of *Gli3* alone (Sheth et al., 2012). In E10.5 $Vps25^{ENU/ENU}$ hindlimb, AER-*Fgf4* was expanded anteriorly (Figures 3A), while ZPA-*Shh* expression was not perturbed (Figure 3B). At E11–11.5,

Vps25$^{ENU/ENU}$ hindlimb *Fgf4* and mesenchymal *Gremlin* (Verheyden and Sun, 2008) were expanded anteriorly (Figures 3C,3D, S3A) as was *Shh* expression, while *Fgf8* was unperturbed (Figure 3E). Consistent with ZPA-*Shh* expansion, *Patched1* was up-regulated in E11.5 *Vps25*$^{ENU/ENU}$ hindlimb (Figure 3F). Moreover, significantly increased *Shh* and *Patched1* mRNA levels were detected by qRT-PCR in E11.5 *Vps25*$^{ENU/ENU}$ *versus* WT hindlimbs (Figure 3G,3H). In addition, Western blot on whole limb lysates demonstrated greater reduction of Gli3 repressor (Gli3R) (Wang et al., 2000) levels in *Vps25*$^{ENU/ENU}$ hindlimb (Figures 3I, S3B) *versus* forelimb (Figure S3C). Furthermore, in E11.5 *Vps25*$^{ENU/ENU}$ anterior hindlimb, ectopic expression of *Hand2*, *HoxD13* and *Gli1*, as well as down-regulation of *Gli3*, were observed before *Shh* ectopic anterior expression could be detected at E12-12.5 (Figure 3J–3N). Of note, in E12.5 mutant hindlimb, *Shh* persisted in the ZPA (Figure 3N), *Fgf4* and *Fgf8* were still present in anterior AER (Figure 3O,3P), and *Sprouty2* was therein up-regulated (Figure 3Q). Also, ectopic *Gli1* and *HoxD13* were still manifest in E12.5 *Vps25*$^{ENU/ENU}$ hindlimb (Figure S3D,S3E). Intriguingly, while BMP activity is required to regulate digit number (Selever et al., 2004), early BMP as well as WNT signaling components (Zeller, 2010) appeared unperturbed in E11 mutant hindlimbs (Figure S3F–S3K). These results establish selective enhancement of the FGF-SHH cross-signaling loop in *Vps25*$^{ENU/ENU}$ limb patterning.

The WT ESCRT-II/Vps25-ESCRT-III/Vps20 complex is mostly detected within late endosomes, while the mutant Vps25^{ENU}-Vps20 complex is diffuse throughout the cytoplasm

To test whether the 9 amino acid insertion into the Vps25^{ENU} protein in mutant embryos led to perturbed function, we assessed cellular localization of transfected Flag- or HA-tagged WT and *Vps25*^{ENU} cDNA constructs expressed alone or in combination. Regardless of the tag, WT and Vps25^{ENU} proteins co-localized within the cytoplasm, also within distinct puncta (Figure 4A–4G). Co-immunoprecipitation of WT and Vps25^{ENU} proteins by tag-specific antibodies followed by Western blotting with an anti-Vps25 antibody (Langelier et al., 2006) showed that Vps25 ENU-induced mutation does not inhibit heterodimerization of Vps25 mutant protein with WT (Figure 4H). Furthermore, co-transfected WT or Vps25^{ENU} proteins co-localized within the cytoplasm and co-immunoprecipitated with Vps20, a component of the ESCRT-III complex that binds to ESCRT-II via its Vps25 subunit (Babst et al., 2002a; Im et al., 2009), suggesting that both WT and Vps25^{ENU} proteins can recruit Vps20 (Figure 4I–4O). Given co-localization with the late endosome marker Lamp1 (Shim et al., 2006), but not EEA1, which stains early endosomes, cytoplasmic puncta containing either WT or mutant Vps25-Vps20 complex are late endosomes (Figure S4). However, while the WT Vps25-Vps20 protein complex was predominantly localized within late endosomes, the mutant Vps25^{ENU}-Vps20 complex appeared mostly diffuse throughout the cytoplasm (Figure 4I–4N). Since interactions between ESCRT-II and ESCRT-III are critical for scission of cargo-filled vesicles into the developing endosome (Im et al., 2009), mislocalization of the mutant complex likely contributes to disruption of vesicular trafficking.

Structural rigidification of the Vps25^{ENU} protein underlies abnormal subcellular localization of the mutant ESCRT-II/ESCRT-III complex with perturbed lysosome-mediated trafficking and impaired degradation of cargo

To determine whether the 9 amino acid insertion (Figure 1G) affects the conformation and dynamics of the mutant protein, we used computational modeling of the Vps25^{ENU} protein structure. In three separate simulations of Vps25 WT and mutant proteins, the WH2 domain (Im and Hurley, 2008) in Vps25^{ENU} was found to be less flexible than in WT (Figures 5A, S5A–S5C). Analyses of conformational changes and fluctuations identified a new stabilizing hydrogen bond in Vps25^{ENU} between a residue from the ENU-induced insertion, Ser (IV), and Glu (105+9) (Figures 5A, S5D). The structural context observed from the simulations attributes the greater conformational stability of the Vps25^{ENU} protein to the presence of stronger hydrogen bonds, one of which cannot form in the Vps25^{WT}. The increased rigidity of the Vps25^{ENU} framework might be unable to conform to the characteristic Y-shaped structure typical of ESCRT-II (Teis et al., 2010). Such a structural rigidification of the Vps25^{ENU} protein could potentially change its overall interaction with other ESCRT-II components like Vps22 and Vps36, as well as interactions with ESCRT-III (Im et al., 2009). While Vps20/ESCRT-III is recruited to Vps25^{ENU}/ESCRT-II, the subcellular localization of the mutant Vps25^{ENU}–Vps20 complex is altered (Figures 4, S4), suggesting perturbed degradation of signaling molecules.

To evaluate whether the *Vps25* ENU-induced mutation caused abnormal lysosome-mediated trafficking and degradation of cargo within the cell, we isolated mouse embryonic fibroblasts (MEFs) from WT and *Vps25$^{ENU/ENU}$* embryos. Transmission electron microscopy (TEM) revealed significantly enlarged Multivesicular Bodies [MVBs, a form of late endosomes (Henne et al., 2011 & 2013)] in mutant *versus* WT MEFs (Figure 5B–5D). Horseradish peroxidase (HRP) uptake experiments (Shim et al., 2006) followed by TEM showed that in *Vps25$^{ENU/ENU}$* MEFs there are significantly higher numbers of HRP-positive MVBs than HRP-positive lysosomes (Figure 5E). Accordingly, in *Vps25$^{ENU/ENU}$* MEFs HRP-positive lysosomes were negligible (Figure 5F). HRP pulse-chase experiments followed by Western blotting with an anti-HRP Ab confirmed HRP degradation defects in *Vps25$^{ENU/ENU}$* MEFs (Figure 5G). Importantly, TEM revealed significantly enlarged MVBs also *in vivo* in limb bud AER as well as mesenchyme of E11.5 *Vps25$^{ENU/ENU}$* embryos *versus* WT littermates (Figure 5H–5K). Altogether, these results indicate that in WT MEFs exogenous HRP is trafficked to lysosomes via MVBs, while in *Vps25$^{ENU/ENU}$* MEFs HRP does not reach lysosomes for degradation and is trapped in engorged MVBs. The latter are significantly enlarged in cultured mutant MEFs and also in mutant limb bud compartments, demonstrating that similar abnormalities occur *in vivo* as a result of *Vps25* mutation.

In *Vps25$^{ENU/ENU}$* mouse embryonic fibroblasts, pFGFR retained within late endosomes leads to increased levels of FGF second messengers, while SHH signaling remains unperturbed

To assess whether perturbed degradation generated enhancement of FGF and/or SHH signaling in a cellular system, as in *Vps25$^{ENU/ENU}$* mutant limbs, we analyzed components of both pathways in WT and mutant MEFs. Pearson's coefficient analysis (Teis et al., 2008) of FGF4 pulse-chase experiments showed a 1.3-fold increase in co-localization of pFGFR

and Lamp1 in *Vps25*$^{ENU/ENU}$ MEFs *versus* WT (Figure 6A–6G). Additionally, LysoTracker staining (Shim et al., 2006), which measures vesicular pH, was decreased by approximately 50% in *Vps25*$^{ENU/ENU}$ MEFs *versus* WT after FGF4 pulse-chase (Figure 6H–6J), supporting a defect in lysosomal functionality. Also, in WT MEFs, phospho-ERK (pERK) decreased within one hour of cycloheximide (CHX) treatment, while in *Vps25*$^{ENU/ENU}$ MEFs pERK levels, which were already higher than in WT before treatment, remained elevated for 2.5 hours, indicating abnormal endosome-mediated degradation (Figure 6K,6L). Consistent with accumulation of pFGFR in *Vps25*$^{ENU/ENU}$ MEFs, we observed higher pERK and pSTAT3 (Hart et al., 2000) levels in E13.5 mutant whole embryos and E11.5 mutant *versus* WT limbs (Figure 6M). Kinetics of pSTAT3 activation *versus* degradation, in FGF pulse-chase experiments, revealed higher pSTAT3 levels in *Vps25*$^{ENU/ENU}$ MEFs *versus* WT (Figure 6N,6O). In contrast, relative expression of SHH pathway components *Gli1* and *Patched1* was not significantly perturbed in *Vps25*$^{ENU/ENU}$ MEFs untreated or stimulated with the SHH agonist SAG (Goetz et al., 2009) *versus* WT (Figure 7A,7B). Accordingly, Smoothened, a transducer of SHH signaling, did not accumulate in the engorged late endosomes of *Vps25*$^{ENU/ENU}$ MEFs (Figure 7C). Pearson's coefficient analysis of Smoothened trafficking in MEFs showed no co-localization of Smoothened and engorged Lamp1-positive endosomes in *Vps25*$^{ENU/ENU}$ MEFs untreated or stimulated with SAG (Figure 7D). Together, these results demonstrate that in *Vps25*$^{ENU/ENU}$ MEFs pFGFR is retained in late endosomes and does not reach lysosomes for degradation. Furthermore, FGF second messengers pERK and pSTAT3 are increased in *Vps25*$^{ENU/ENU}$ embryos and MEFs, highlighting FGF signaling up-regulation in both systems. Unexpectedly, SHH signaling is not intrinsically upregulated in *Vps25*$^{ENU/ENU}$ MEFs and SHH pathway components do not accumulate within late endosomes, suggesting that SHH enhancement in mutant limbs results from selective hyperactive FGF signaling within the FGF-SHH feedback loop.

Inhibition of the FGF-SHH signaling loop via reduction of SHH dosage rescues polydactyly in *Vps25*$^{ENU/ENU}$ limbs

To determine whether polydactyly could be specifically ameliorated by limiting FGF-SHH cross-signaling in *Vps25*$^{ENU/ENU}$ embryos, we reduced the dosage of SHH (Chiang et al., 2001). Genetic reduction of SHH in *Vps25*$^{ENU/ENU}$*;Shh*$^{+/-}$ mutants partially rescued polydactyly (Figures 7E, S7A) by preventing *Fgf4* expansion present in *Vps25*$^{ENU/ENU}$ anterior hindlimb AER (Figure 7E′; see also Figure 3A,3C,3D). Seven digit-hindlimbs decreased from 39% in *Vps25*$^{ENU/ENU}$ mutant embryos to 14% in *Vps25*$^{ENU/ENU}$*;Shh*$^{+/-}$ mutants, and pentadactyly, albeit with abnormally shaped digits, appeared in 27% of *Vps25*$^{ENU/ENU}$*;Shh*$^{+/-}$ hindlimbs (Figure S7B). Partial genetic rescue of polydactyly in *Vps25*$^{ENU/ENU}$*;Shh*$^{+/-}$ limbs demonstrates that ESCRT-II/Vps25 constrains digit number by specific modulation of the FGF-SHH cross-regulatory loop in the limb. Remarkably, loss of 1 allele of *Shh* did not partially rescue the craniofacial defects of *Vps25*$^{ENU/ENU}$ embryos, consisting of hypoplastic jaw, stunted snout, and malformed ear pinna (Figure S7C). These findings strongly underscore that the Vps25 ENU-induced mutation preferentially and primarily affects FGF signaling in the limb bud and that SHH enhancement in *Vps25*$^{ENU/ENU}$ mutant limbs results from hyperactivation of FGF signaling within the FGF-SHH feedback loop (Figure 7F,7G).

Discussion

ESCRT complex components, first identified in yeast, control multiple cellular functions, including receptor signaling, cytokinesis, autophagy, cell migration/motility, repair of plasma membrane wounds, miRNA activity, and mRNA localization/transport in metazoans (Henne et al., 2013; Jimenez et al., 2014; Rusten et al., 2012). Evidence supports requirements of ESCRT proteins in promoting endosome-mediated degradation of signaling receptors across the animal kingdom (MacGurn et al., 2012; Rusten et al., 2012). However, despite their reported roles in signal attenuation, in *Drosophila* Vps27/Hrs-Stam (ESCRT-0) promotes FGF signaling (Chanut-Delalande et al., 2010) and in *Xenopus* Vps4 acts as a positive regulator of WNT signaling (Taelman et al., 2010). This suggests a yet unexplored diversity in the regulation of signaling by ESCRT components. Consistent with constitutive expression of ESCRT subunits and with their pleiotropic roles in trafficking of signaling proteins, LOF mutations of mouse ESCRT components result in early lethality *in utero* (E8-11) (Rusten et al., 2012). This has precluded dissection of specific ESCRT-dependent morphogenetic processes during organ formation. Here, the ENU-induced hypomorphic mutation of murine ESCRT-II/Vps25 results in late embryonic lethality, thus affording deconstruction of unexplored ESCRT-II requirements in the control of signal transduction underlying mammalian tissue patterning. Using this unique model, we propose that ESCRT-II/Vps25 constrains digit number by exerting selective attenuation of FGF signaling and by consequently maintaining homeostasis of the FGF-SHH feedback loop in the developing limb. Interestingly, together with hyperactivation of FGF-SHH signaling in mutant $Vps25^{ENU/ENU}$ limbs, *Fgf* and *Shh* mRNAs are also upregulated suggesting a direct or indirect positive feedback whereby the increased protein levels cause upregulation of their own mRNAs. Alternatively, since ESCRT-II can directly affect mRNA localization acting as RNA binding proteins, ESCRT-II/Vps25 mutations might yield accumulation of select mRNAs within the cell (Irion and St Johnston, 2007). Lastly, mutations of Vps25/ESCRT-II might directly affect miRNA-mediated degradation of specific mRNAs (Gibbings et al., 2009), potentially including *Fgf* and *Shh*, in mutant limbs.

FGF signaling mediates multiple functions in embryonic development (Goetz and Mohammadi, 2013; Itoh and Ornitz, 2004). In limb bud mesenchyme, FGF4 stimulates proliferation (Niswander and Martin, 1993) and, together with FGF8, is required for cell survival (Sun et al., 2002). While multiple reports link polydactyly to ectopic or enhanced SHH activity (Anderson et al., 2012), increased *Fgf4* expression in early mouse limbs causes polydactyly (Lu et al., 2006) and ectopic *Fgf4* expression in spontaneous mutant chickens initiates polydactyly independent of SHH activity (Bouldin and Harfe, 2009). Interestingly, $Vps25^{ENU/ENU}$ mutant hindlimbs exhibit *Fgf4* expansion before *Shh* perturbations arise, which alone could result in enhanced proliferation and lack of cell death causing polydactyly. FGF signaling has also critical roles in the control of endochondral bone development (Chen et al., 2014; Ornitz and Marie, 2002). Notably, limbs of $Vps25^{ENU/ENU}$ embryos display abnormally short and thick skeletal elements (Figures 2A,2B, S2F–S2L′), similar to humans with achondroplasia (dwarfism) (Ornitz and Marie, 2002). Achondroplastic patients and mouse models harboring activating mutations of the FGF pathway exhibit skeletal hypoplasia and epiphyseal growth plate dysmorphology (Naski et

al. 1998). Due to edema and hemorrhaging in *Vps25*$^{ENU/ENU}$ embryos already at E14.0, it is impossible to determine whether their skeletal hypoplasia is due to cell-autonomous FGF activation in the growth plate until a mouse with *Vps25* conditional LOF is available. Nonetheless, the striking similarities of the skeletal phenotypes in these mouse mutants support a scenario whereby *Vps25* mutation disrupts bone development by perturbing FGF signaling, leading to achondroplastic phenotypes.

Intriguingly, in the developing limb not all signaling pathways are hyperactive, or otherwise altered, as a result of ESCRT-II complex impairment. For example, in *Vps25*$^{ENU/ENU}$ limbs at E11, when FGF signaling is hyperactive, early WNT and BMP signaling components appear unperturbed. This is worthy of note, since proper BMP activity is required to regulate digit number (Selever et al., 2004). In addition, in *Vps25*$^{ENU/ENU}$ mouse embryonic fibroblasts FGF signaling is up-regulated, while SHH signaling is not intrinsically enhanced. Lastly, in *Vps25*$^{ENU/ENU}$ embryos, loss of 1 allele of *Shh* partially rescues polydactyly by preventing *Fgf4* expansion, whereas it does not partially rescue the craniofacial defects. Together, the findings in this model underscore preferential hyperactivation of FGF signaling as the main culprit of polydactyly in ESCRT-II/Vps25 mutant embryos. Alternatively, these results could suggest that during early limb patterning maintenance of homeostasis of most signaling pathways requires relatively low levels of ESCRT-II function, with a few exceptions such as the FGF pathway for which ESCRT function would become rate-limiting in a context-specific manner. On the other hand, since Vps25 has been shown to control Notch and other signaling pathways in *Drosophila* (Thompson et al., 2005; Vaccari and Bilder, 2005), signaling cascades other than FGF might be affected in other domains of *Vps25*$^{ENU/ENU}$ embryos. In addition, within the limb bud proper, signaling mediated by other tyrosine kinase receptors might be concomitantly enhanced in *Vps25*$^{ENU/ENU}$ embryos and might contribute to polydactyly. In particular, expression of constitutively active EGFR in chick limbs *in ovo* causes polydactyly (Omi et al., 2005). Yet, in contrast to *Vps25*$^{ENU/ENU}$ embryos, developing limb buds with activated EGFR exhibit multiple, fragmented, or bifurcating ectopic AERs expressing *Fgf8*, as well as down-regulation of *Bmp4*, resulting in pre- and post-axial polydactyly.

In summary, we isolated an ENU-induced hypomorphic mutation of ESCRT-II/Vps25 in a polydactylous mouse line, which allowed dissection of the mechanisms whereby ESCRT components execute mammalian limb patterning. The availability of this unique mouse model led us to establish that in the developing embryo ubiquitously expressed ESCRT machineries act on different receptors and associated signaling proteins in a preferential manner. In addition, our study demonstrates that ESCRT-mediated down-regulation of specific signaling pathways appears more critical in certain embryonic contexts than in others. While limb, craniofacial, and heart development are severely affected by the ESCRT-II/Vps25 mutation, development of other organ systems appears unperturbed. Our research demonstrates that ESCRT-II/Vps25 effects preferential modulation of FGF signaling in the mammalian limb, which, in turn, controls cellular proliferation and cell death establishing normal digit number and identity, as well as controlling skeletal maturation, relevant to congenital limb defects. Broadly, our study proposes a mechanism for signaling homeostasis in the vertebrate embryo highlighting that endosomal sorting by

specific components of the ESCRT machinery preferentially regulates, or is rate-limiting for, select conserved signaling pathways in distinct tissue patterning processes.

Experimental Procedures

A detailed description of reagents and protocols is in the Supplemental Experimental Procedures. See the following Experimental Procedures for brief descriptions.

Generation of Mutant Line *04-014* by a N-ethyl-N-nitrosourea Mutagenesis Screen

Mutant mouse line *04-014* was generated by ENU-mutagenesis of C57BL/6J males, as previously described (Anderson and Ingham, 2003; Stottmann and Beier, 2010).

High-resolution Mapping and Transcriptome Analysis for Gene Cloning

To clone the gene responsible for the ENU-induced mutation, classic procedures combining whole-genome Single Nucleotide Polymorphism (SNP) (Moran et al., 2006) mapping with gene expression microarray analysis for gene finding were used. Total RNA from E12.5 WT and homozygous mutant embryos from line *04-014* was purified using the RNeasy kit (QIAGEN). Roche NimbleGen 12plex HD2 gene expression microarrays (Design number 100718_MM9 _exp_HX12) were used to analyze expression of all genes within the narrowest critical interval (500 kb) linked to the ENU-induced mutation. cDNA from total RNA was amplified/labeled using Cy3-coupled random nonamers. Technical triplicate hybridizations were performed per sample. Hybridizations were conducted using 4 ug of labeled cDNA per subarray, as per the Roche NimbleGen Gene Expression Protocol. The array data were analyzed using ArrayStar software version 4.0.2 (DNASTAR, INC. Madison, WI). Both the mutant and control technical replicates were normalized together, and P values were generated for all expression changes. Pairwise comparisons of global gene expression calls between any two of the technical triplicates per sample correlated with R-squared values of greater than 0.97.

Custom Sureselect Capture and SOLiD Sequencing

DNA capture was performed on 3μg of high quality genomic DNA using a custom SureSelect Target Enrichment kit (protocol by Agilent). Chromosome 11 enriched DNA libraries were sequenced on a SOLiD 3plus system (Life Technologies). 22 million reads were generated; 79.7% of the reads were on target and 95.3% of the target was covered at 10X.

Phenotypic Analysis of *04-014* Embryos

Skeletal preparations, *in situ* hybridizations, X-Gal stainings and OPT imaging were carried out as described (Ferretti et al., 2011; Sharpe et al., 2002).

Proliferation and Apoptosis Assays

Protocols were as described (Ferretti et al., 2011).

mRNA Isolation, RT- PCR, qRT-PCR

Total RNA was purified from embryos, embryonic limbs, or Mouse Embryonic Fibroblasts (MEFs) at E10.5-E13.5 using standard procedures. Gene expression was determined by quantitative real-time PCR using QuantiTect SYBR Green PCR master mix (Qiagen) or pre-designed TaqMan Gene expression Assays and the 7500 Real-Time PCR System (Applied Biosystems).

Generation of *Vps25* Global LOF Allele

Vps25 global LOF was obtained by insertion of a *LacZ* cassette into the gene locus ($Vps25^{tm1(KOMP)Vlcg/+}$) (trans-NIH Knock-Out Mouse Project - KOMP). All animal experiments were performed following protocols approved by the WCMC IACUC.

Immunohistofluorescence and Whole-mount LysoTracker

Embryos were cryosectioned for immunofluorescence (IF) experiments or incubated with LysoTracker (Naiche and Papaioannou, 2007) to detect whole-mount staining.

Cell Culture

MEFs were isolated according to standard protocols from E11.5-13.5 WT and $Vps25^{ENU/ENU}$ embryos. MEFs were pulse-chased with FGF4 for various time points as indicated or treated for 24 hours with SAG (Goetz et al., 2009) and tested for different markers by IF and qRT-PCR. Cell trafficking was investigated by LysoTracker staining and Horseradish Peroxidase (HRP) uptake experiments (Shim et al., 2006). For HRP uptake experiments, cells were incubated with 100 μg/mL HRP for 1 hour, then chased for different times as indicated. For HRP uptake experiments followed by Transmission Electron Microscopy (TEM), cells were serum starved prior to stimulation with 5 mg/mL HRP for 30 min, then fixed and crosslinked with 3,3′-Diaminobenzidine (DAB), and prepared for TEM. The protein synthesis inhibitor Cycloheximide (CHX) was used to treat MEFs (50 μg/ml) as indicated, in order to examine pERK protein degradation, after which cells were lysed for Western blotting (WB).

In vitro Transient Transfection Assays

HEK293 were cultured in DMEM supplemented with 10% fetal calf serum, 2 mM L-glutamine (Invitrogen), in humidified 5% CO2. Transient transfections were performed using LT1 reagent (Mirus) at a 5:2 ratio. Cells were fixed for immunostaining or harvested in NP40 buffer for co-immunoprecipitation (IP) 36 hours after transfection.

Immunoprecipitations and Western Blot Analysis

HEK293 cells were transfected with HA- or FLAG-tagged constructs to conduct IP and WB using HA (mouse/Covance, goat/Santa Cruz) or FLAG (Sigma) Ab. For IP and co-IP, cells were lysed in NP40 and incubated overnight with appropriate primary Ab, magnetic beads were applied for 2 hours, then complexes were dissociated using DTT before WB analysis. WB was performed using whole embryos, limbs, MEFs, or HEK293 cells. Samples were lysed in RIPA buffer and proteins separated on a 4–12% precast gel followed by transfer to

0.2% nitrocellulose membranes. Primary Abs were incubated in blocking solution overnight at 4°C and blotted with the relevant secondary Abs.

Computational Approach to 3D Modeling of Vps25^{WT} and Vps25^{ENU} Mutant Proteins

For computational modeling and simulation studies designed to distinguish differences in structure and dynamics between Vps25^{WT} and Vps25^{ENU}, the molecular models of the two constructs were immersed in a restrained water sphere (Phillips et al., 2005) for extensive dynamics simulations. Six separate simulations were done, consisting of triplicate repeats for Vps25^{WT} and Vps25^{ENU}.

Transmission Electron Microscopy

MEFs and isolated limb buds were processed following standard procedures (Venable and Coggeshall, 1965). 2 WT and 5 *Vps25*$^{ENU/ENU}$ mutant embryos at E11.5 were imaged to visualize MVBs in limb AER and mesenchyme compartments. MVB diameters measured using ImageJ64 and MatLab (MathWorks Inc.).

Statistical Analysis

Results are given as the average ± standard deviation (SD) or standard error of mean (SEM). Statistical analyses were performed with Excel (Microsoft Corp.) applying the two-tailed t test. P values below 0.05 were considered significant.

Calculation of Pearson's Coefficient

MatLab (MathWorks Inc.) was used to calculate co-localization of IF signals.

Supplementary Material

Refer to Web version on PubMed Central for supplementary material.

Acknowledgments

Study funded by grants R21DE018031, R21DE018031-02S1 and 2R01HD043997 to L.S. ES cell clones with Vps25 LOF obtained from KOMP. NIH grants to Velocigene at Regeneron Inc. (U01HG004085) and the CSD Consortium (U01HG004080) funded the generation of gene-targeted ES cells for 8500 genes (KOMP Program) distributed by UC Davis and CHORI (U42RR024244). We thank David Beier, Jennifer Moran, and Tim McGraw for stimulating discussions; Wesley I. Sundquist for invaluable suggestions and the generous gift of a VPS25 polyclonal antibody; Leona Cohen-Gould for TEM; Agnes Viale and Nicholas D. Socci for deep sequencing; Mu He for technical suggestions. Thanks to Robert Aho for data analyses and artwork composition.

References

Anderson E, Peluso S, Lettice LA, Hill RE. Human limb abnormalities caused by disruption of hedgehog signaling. Trends Genet. 2012; 28:364–373. [PubMed: 22534646]

Anderson KV, Ingham PW. The transformation of the model organism: a decade of developmental genetics. Nat Genet. 2003; 33:285–293. [PubMed: 12610538]

Arnold CN, Xia Y, Lin P, Ross C, Schwander M, Smart NG, Muller U, Beutler B. Rapid identification of a disease allele in mouse through whole genome sequencing and bulk segregation analysis. Genetics. 2011; 187:633–641. [PubMed: 21196518]

Babst M, Katzmann DJ, Estepa-Sabal EJ, Meerloo T, Emr SD. Escrt-III: an endosome-associated heterooligomeric protein complex required for mvb sorting. Dev Cell. 2002a; 3:271–282. [PubMed: 12194857]

Babst M, Katzmann DJ, Snyder WB, Wendland B, Emr SD. Endosome-associated complex, ESCRT-II, recruits transport machinery for protein sorting at the multivesicular body. Dev Cell. 2002b; 3:283–289. [PubMed: 12194858]

Biesecker LG. Polydactyly: how many disorders and how many genes? 2010 update. Dev Dyn. 2011; 240:931–942. [PubMed: 21445961]

Bouldin CM, Harfe BD. Aberrant FGF signaling, independent of ectopic hedgehog signaling, initiates preaxial polydactyly in Dorking chickens. Dev Biol. 2009; 334:133–141. [PubMed: 19616534]

Chanut-Delalande H, Jung AC, Baer MM, Lin L, Payre F, Affolter M. The Hrs/Stam complex acts as a positive and negative regulator of RTK signaling during Drosophila development. PloS One. 2010; 5:e10245. [PubMed: 20422006]

Chen P, Zhang L, Weng T, Zhang S, Sun S, Chang M, Li Y, Zhang B, Zhang L. A Ser252Trp mutation in fibroblast growth factor receptor 2 (FGFR2) mimicking human Apert syndrome reveals an essential role for FGF signaling in the regulation of endochondral bone formation. PLoS One. 2014; 9(1):e87311. [PubMed: 24489893]

Chiang C, Litingtung Y, Harris MP, Simandl BK, Li Y, Beachy PA, Fallon JF. Manifestation of the limb prepattern: limb development in the absence of sonic hedgehog function. Dev Biol. 2001; 236:421–435. [PubMed: 11476582]

Ferretti E, Li B, Zewdu R, Wells V, Hebert JM, Karner C, Anderson MJ, Williams T, Dixon J, Dixon MJ, et al. A conserved Pbx-Wnt-p63-Irf6 regulatory module controls face morphogenesis by promoting epithelial apoptosis. Dev Cell. 2011; 21:627–641. [PubMed: 21982646]

Gibbings DJ, Ciaudo C, Erhardt M, Voinnet O. Multivesicular bodies associate with components of miRNA effector complexes and modulate miRNA activity. Nat Cell Biol. 2009; 11:1143–1149. [PubMed: 19684575]

Goetz R, Mohammadi M. Exploring mechanisms of FGF signalling through the lens of structural biology. Nat Rev Mol Cell Biol. 2013; 14:166–180. [PubMed: 23403721]

Goetz SC, Ocbina PJ, Anderson KV. The primary cilium as a Hedgehog signal transduction machine. Methods Cell Biol. 2009; 94:199–222. [PubMed: 20362092]

Hart KC, Robertson SC, Kanemitsu MY, Meyer AN, Tynan JA, Donoghue DJ. Transformation and Stat activation by derivatives of FGFR1, FGFR3, and FGFR4. Oncogene. 2000; 19:3309–3320. [PubMed: 10918587]

Henne WM, Buchkovich NJ, Emr SD. The ESCRT pathway. Dev Cell. 2011; 21:77–91. [PubMed: 21763610]

Henne WM, Stenmark H, Emr SD. Molecular mechanisms of the membrane sculpting ESCRT pathway. Cold Spring Harb Perspect Biol. 2013; 5(9)

Im YJ, Hurley JH. Integrated structural model and membrane targeting mechanism of the human ESCRT-II complex. Dev Cell. 2008; 14:902–913. [PubMed: 18539118]

Im YJ, Wollert T, Boura E, Hurley JH. Structure and function of the ESCRT-II-III interface in multivesicular body biogenesis. Dev Cell. 2009; 17:234–243. [PubMed: 19686684]

Irion U, St Johnston D. bicoid RNA localization requires specific binding of an endosomal sorting complex. Nature. 2007; 445:554–558. [PubMed: 17268469]

Itoh N, Ornitz DM. Evolution of the *Fgf* and *Fgfr* gene families. Trends Genet. 2004; 20:563–569. [PubMed: 15475116]

Jimenez AJ, Maiuri P, Lafaurie-Janvore J, Divoux S, Piel M, Perez F. ESCRT machinery is required for plasma membrane repair. Science. 2014; 343(6174):1247136. [PubMed: 24482116]

Komada M, Soriano P. Hrs, a FYVE finger protein localized to early endosomes, is implicated in vesicular traffic and required for ventral folding morphogenesis. Genes Dev. 1999; 13:1475–1485. [PubMed: 10364163]

Koss M, Bolze A, Brendolan A, Saggese M, Capellini TD, Bojilova E, Boisson B, Prall OW, Elliott DA, Solloway M, et al. Congenital asplenia in mice and humans with mutations in a Pbx/Nkx2-5/p15 module. Dev Cell. 2012; 22:913–926. [PubMed: 22560297]

Lallemand Y, Bensoussan V, Cloment CS, Robert B. Msx genes are important apoptosis effectors downstream of the Shh/Gli3 pathway in the limb. Dev Biol. 2009; 331:189–198. [PubMed: 19422820]

Langelier C, von Schwedler UK, Fisher RD, De Domenico I, White PL, Hill CP, Kaplan J, Ward D, Sundquist WI. Human ESCRT-II complex and its role in human immunodeficiency virus type 1 release. J Virol. 2006; 80:9465–9480. [PubMed: 16973552]

Lee JA, Beigneux A, Ahmad ST, Young SG, Gao FB. ESCRT-III dysfunction causes autophagosome accumulation and neurodegeneration. Curr Biol. 2007; 17:1561–1567. [PubMed: 17683935]

Lopez-Rios J, Speziale D, Robay D, Scotti M, Osterwalder M, Nusspaumer G, Galli A, Hollander GA, Kmita M, Zeller R. GLI3 constrains digit number by controlling both progenitor proliferation and BMP-dependent exit to chondrogenesis. Dev Cell. 2012; 22:837–848. [PubMed: 22465667]

Lu P, Minowada G, Martin GR. Increasing Fgf4 expression in the mouse limb bud causes polysyndactyly and rescues the skeletal defects that result from loss of Fgf8 function. Development. 2006; 133:33–42. [PubMed: 16308330]

MacGurn JA, Hsu PC, Emr SD. Ubiquitin and membrane protein turnover: from cradle to grave. Annu Rev Biochem. 2012; 81:231–259. [PubMed: 22404628]

Mariani FV, Martin GR. Deciphering skeletal patterning: clues from the limb. Nature. 2003; 423:319–325. [PubMed: 12748649]

Moran JL, Bolton AD, Tran PV, Brown A, Dwyer ND, Manning DK, Bjork BC, Li C, Montgomery K, Siepka SM, et al. Utilization of a whole genome SNP panel for efficient genetic mapping in the mouse. Genome Res. 2006; 16:436–440. [PubMed: 16461637]

Naiche L, Papaioannou VE. Cre activity causes widespread apoptosis and lethal anemia during embryonic development. Genesis. 2007; 45:768–775. [PubMed: 18064676]

Naski MC, Colvin JS, Coffin JD, Ornitz DM. Repression of hedgehog signaling and BMP4 expression in growth plate cartilage by broblast growth factor receptor 3. Development. 1998; 125:4977–4988. [PubMed: 9811582]

Niswander L, Martin GR. FGF-4 and BMP-2 have opposite effects on limb growth. Nature. 1993; 361:68–71. [PubMed: 8421496]

Omi M, Fisher M, Maihle NJ, Dealy CN. Studies on epidermal growth factor receptor signaling in vertebrate limb patterning. Dev Dyn. 2005; 233:288–300. [PubMed: 15778992]

Ornitz DM, Marie PJ. FGF signaling pathways in endochondral and intramembranous bone development and human genetic disease. Genes Dev. 2002; 16:1446–1465. [PubMed: 12080084]

Phillips JC, Braun R, Wang W, Gumbart J, Tajkhorshid E, Villa E, Chipot C, Skeel RD, Kale L, Schulten K. Scalable molecular dynamics with NAMD. J Comput Chem. 2005; 26:1781–1802. [PubMed: 16222654]

Ruland J, Sirard C, Elia A, MacPherson D, Wakeham A, Li L, de la Pompa JL, Cohen SN, Mak TW. p53 accumulation, defective cell proliferation, and early embryonic lethality in mice lacking tsg101. Proc Natl Acad Sci U S A. 2001; 98:1859–1864. [PubMed: 11172041]

Rusten TE, Vaccari T, Stenmark H. Shaping development with ESCRTs. Nat Cell Biol. 2012; 14:38–45. [PubMed: 22193162]

Selever J, Liu W, Lu MF, Behringer RR, Martin JF. Bmp4 in limb bud mesoderm regulates digit pattern by controlling AER development. Dev Biol. 2004; 276(2):268–79. [PubMed: 15581864]

Sharpe J, Ahlgren U, Perry P, Hill B, Ross A, Hecksher-Sorensen J, Baldock R, Davidson D. Optical projection tomography as a tool for 3D microscopy and gene expression studies. Science. 2002; 296:541–545. [PubMed: 11964482]

Sheth R, Marcon L, Bastida MF, Junco M, Quintana L, Dahn R, Kmita M, Sharpe J, Ros MA. Hox genes regulate digit patterning by controlling the wavelength of a Turing-type mechanism. Science. 2012; 338:1476–1480. [PubMed: 23239739]

Shim JH, Xiao C, Hayden MS, Lee KY, Trombetta ES, Pypaert M, Nara A, Yoshimori T, Wilm B, Erdjument-Bromage H, et al. CHMP5 is essential for late endosome function and down-regulation of receptor signaling during mouse embryogenesis. J Cell Biol. 2006; 172:1045–1056. [PubMed: 16567502]

Slater R, Bishop NE. Genetic structure and evolution of the Vps25 family, a yeast ESCRT-II component. BMC Evol Biol. 2006; 6:59. [PubMed: 16889659]

Stottmann RW, Beier DR. Using ENU mutagenesis for phenotype-driven analysis of the mouse. Methods Enzymol. 2010; 477:329–348. [PubMed: 20699149]

Sun X, Mariani FV, Martin GR. Functions of FGF signalling from the apical ectodermal ridge in limb development. Nature. 2002; 418:501–508. [PubMed: 12152071]

Tabin C, Wolpert L. Rethinking the proximodistal axis of the vertebrate limb in the molecular era. Genes Dev. 2007; 21:1433–1442. [PubMed: 17575045]

Taelman VF, Dobrowolski R, Plouhinec JL, Fuentealba LC, Vorwald PP, Gumper I, Sabatini DD, De Robertis EM. Wnt signaling requires sequestration of glycogen synthase kinase 3 inside multivesicular endosomes. Cell. 2010; 143:1136–1148. [PubMed: 21183076]

Teis D, Saksena S, Emr SD. Ordered assembly of the ESCRT-III complex on endosomes is required to sequester cargo during MVB formation. Dev Cell. 2008; 15:578–589. [PubMed: 18854142]

Teis D, Saksena S, Judson BL, Emr SD. ESCRT-II coordinates the assembly of ESCRT-III filaments for cargo sorting and multivesicular body vesicle formation. EMBO J. 2010; 29:871–883. [PubMed: 20134403]

Thompson B, Mathieu J, Sung H, Loeser E, Rørth P, Cohen SM. Tumor Suppressor Properties of the ESCRT-II Complex Component Vps25 in Drosophila. Dev Cell. 2005; 9:711–720. [PubMed: 16256745]

Tognon E, Wossner N, Cortese K, Tacchetti C, Vaccari T. ESCRT-0 is not required for ectopic Notch activation and tumor suppression in Drosophila. PLoS One. 2014; 9(4):e93987. [PubMed: 24718108]

Vaccari T, Bilder D. The *Drosophila* Tumor Suppressor *vps25* Prevents Nonautonomous Overproliferation by Regulating Notch Trafficking. Dev Cell. 2005; 9:687–698. [PubMed: 16256743]

Venable JH, Coggeshall R. A simplified lead citrate stain for use in electron microscopy. Journal of Cell Biology. 1965; 25:407–408. [PubMed: 14287192]

Verheyden JM, Sun X. An Fgf/Gremlin inhibitory feedback loop triggers termination of limb bud outgrowth. Nature. 2008; 454:638–641. [PubMed: 18594511]

Wang B, Fallon JF, Beachy PA. Hedgehog-regulated processing of Gli3 produces an anterior/posterior repressor gradient in the developing vertebrate limb. Cell. 2000; 100:423–434. [PubMed: 10693759]

Wolpert L. Do we understand development? Science. 1994; 266:571–572. [PubMed: 7939707]

Yamada M, Ishii N, Asao H, Murata K, Kanazawa C, Sasaki H, Sugamura K. Signal-transducing adaptor molecules STAM1 and STAM2 are required for T-cell development and survival. Mol Cell Biol. 2002; 22:8648–8658. [PubMed: 12446783]

Zakany J, Duboule D. The role of Hox genes during vertebrate limb development. Curr Opin Genet Dev. 2007; 17:359–366. [PubMed: 17644373]

Zeller R. The temporal dynamics of vertebrate limb development, teratogenesis and evolution. Curr Opin Genet Dev. 2010; 20:384–390. [PubMed: 20537528]

Zeller R, Lopez-Rios J, Zuniga Ae. Vertebrate limb bud development: moving towards integrative analysis of organogenesis. Nat Rev Genet. 2009; 10:845–858. [PubMed: 19920852]

Highlights

- ENU-induced mutation of mouse ESCRT-II/Vps25 causes polydactyly
- *Vps25* hypomorphic mutants survive until late gestation unlike ESCRT LOF embryos
- ESCRT-II constrains digit number by endosome-mediated modulation of FGF signaling
- Mutations in ESCRT reveal a novel mechanism underlying congenital limb defects

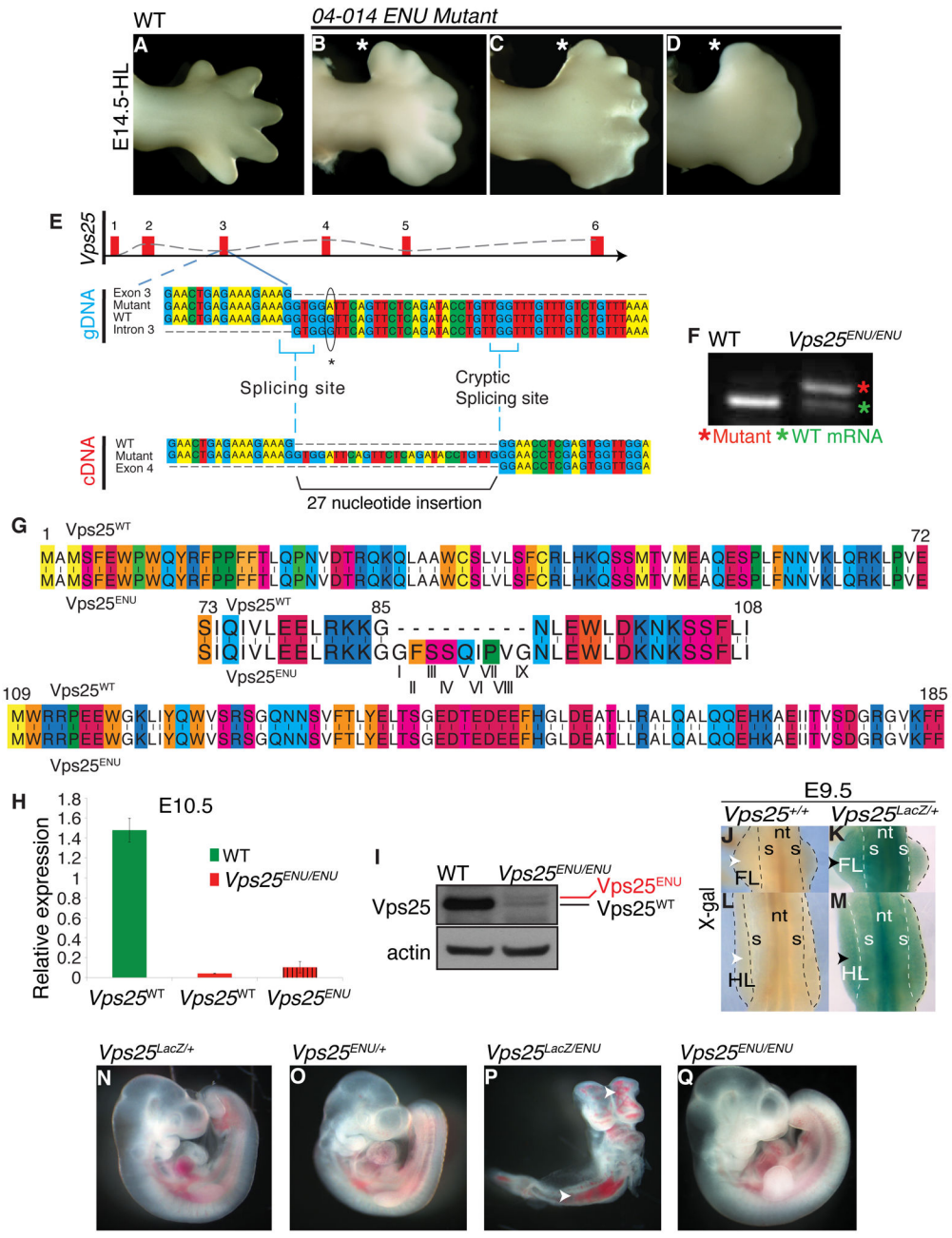

Figure 1. Identification of polydactylous mouse line *04-014* by ENU mutagenesis and cloning of the ESCRT-II/*Vps25* hypomorphic mutation

(A–D) Gross morphology shows different expressivity of the polydactyly in E14.5 *Vps25*$^{ENU/ENU}$ hindlimbs, including a widened autopod with six (B) or seven (C) digits, or synpolydactyly (D) (domain of additional digits; white asterisk).

(E,F) Sequencing of *Vps25* genomic (g) and complementary (c) DNA detects a mutation (asterisk) within intron 3, five nucleotides downstream to the exon-intron border, resulting in a 27 nucleotide insertion in the mutant *Vps25* mRNA, visualized by PCR (F).

(G) Alignment of $Vps25^{WT}$ (top) (Protein UniProt/NCBI number: Q9CQ80) and $Vps25^{ENU}$ mutant (bottom) proteins shows a 9 amino acid insertion starting at amino acid 86. $Vps25^{WT}$ protein contains two winged helix domains WH1 (amino acids 1-84) and WH2 (amino acids 84-176) (Langelier et al., 2006). The additional 9 amino acids, indicated by roman numbers, reside within the Vps25 WH2 domain.

(H,I) qRT-PCR and Western blot (WB) from E10.5 whole embryos demonstrate presence of WT Vps25 mRNA and protein, respectively, in $Vps25^{ENU/ENU}$ mutants. qRT-PCR, mean of 2 samples run in triplicate ± SEM; *Tbp* used for normalization.

(J–M) X-gal staining reveals ubiquitous *Vps25* expression, including forelimb (FL) and hindlimb (HL) (black arrowheads), in E9.5 $Vps25^{LacZ/+}$ embryos, *versus* lack of staining (white arrowheads) in WT. s, somites; nt, neural tube.

(N–Q) Delayed and abnormal development of $Vps25^{LacZ/ENU}$ double heterozygote (arrowheads indicate hemorrhaging) as early as E9.5 *versus* WT morphology of $Vps25^{LacZ/+}$ and $Vps25^{ENU/+}$ single heterozygotes proves that the $Vps25^{ENU}$ mutation is not complemented by the *Vps25* LOF allele. As predicted for a hypomorphic allele, $Vps25^{ENU/ENU}$ embryos survive until later in gestation and appear normal at E10.5 (Q). See also Figure S1, Tables S1,S2,S3.

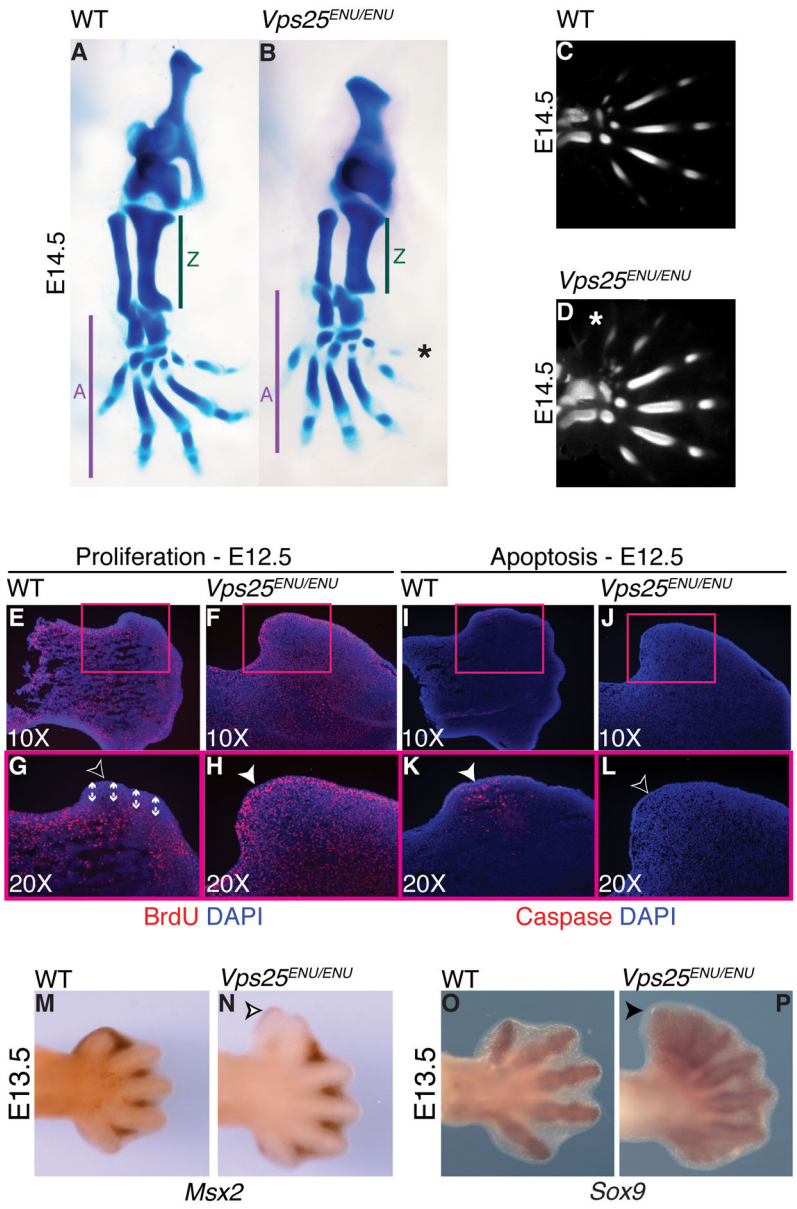

Figure 2. Pre-axial polydactyly, proliferation and apoptosis defects in *Vps25*$^{ENU/ENU}$ mutant hindlimb

(A,B) Shorter and thicker hindlimb (HL) zeugopod (Z) and pre-axial polydactyly (asterisk) in E14.5 *Vps25*$^{ENU/ENU}$ autopod (A) by alcian blue staining.

(C,D) OPT shows polydactyly (asterisk) in E14.5 *Vps25*$^{ENU/ENU}$ HL.

(E–L) BrdU and cleaved Caspase- 3 IF reveals increased proliferation (white arrowhead) and decreased apoptosis (empty arrowhead) in E12.5 *Vps25*$^{ENU/ENU}$ anterior HL.

(M–P) *In situ* hybridization shows loss of *Msx2* (empty arrowhead) and increased *Sox9* (black arrowhead) mRNA in E13.5 *Vps25*$^{ENU/ENU}$ anterior HL. See also Figure S2, Movies S1,S2.

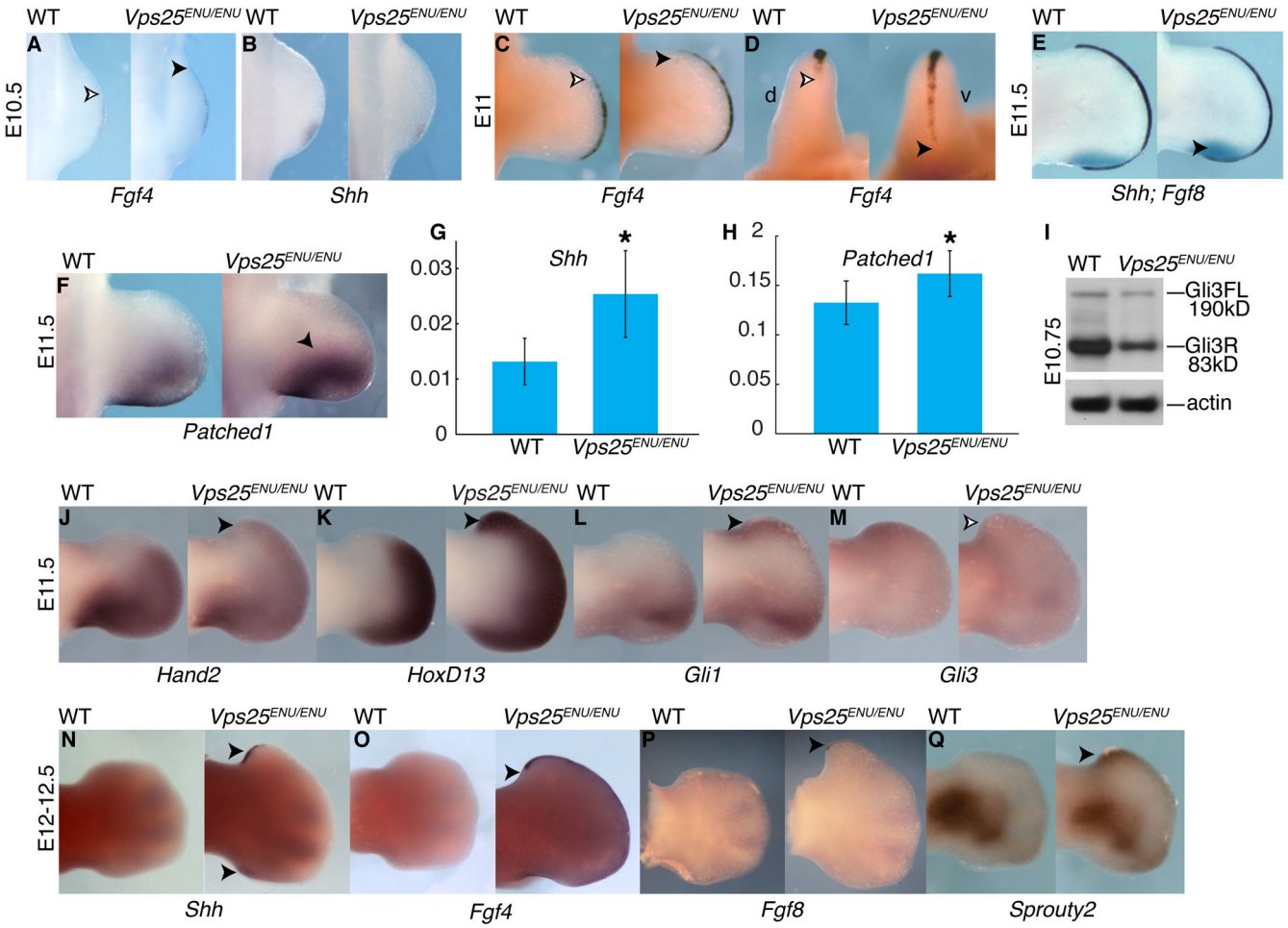

Figure 3. Selective enhancement of the FGF-SHH cross-regulatory loop in *Vps25*$^{ENU/ENU}$ early HL buds

(A–F) Expression of *Fgf4*, *Shh*, *Fgf8*, and *Patched1* by *in situ* hybridization of E10.5-E11.5 WT and *Vps25*$^{ENU/ENU}$ HL buds.

(G,H) qRT-PCR of *Shh* and *Patched1* mRNAs from E11.5 WT and *Vps25*$^{ENU/ENU}$ HL buds; *Rpl19* as internal control. Bars; mean of 3 HL bud pairs run in triplicate ± SD (*, $p<0.05$).

(I) WB demonstrates altered Gli3 processing in E10.75 *Vps25*$^{ENU/ENU}$ HL, wherein levels of Gli3R are reduced. FL,full-length; R, repressor.

(J–Q) Expression of *Hand2*, *HoxD13*, *Gli1*, *Gli3*, *Shh*, *Fgf4*, *Fgf8*, and *Sprouty2* by *in situ* hybridization of E11.5-E12.5 WT and *Vps25*$^{ENU/ENU}$ HL buds.

Anterior, top; proximal, left; d, dorsal; v, ventral; a′, anterior view. Black arrowheads; spatially expanded, temporally protracted, and ectopic gene expression in mutant buds. Empty arrowheads; absence of signal. See also Figure S3.

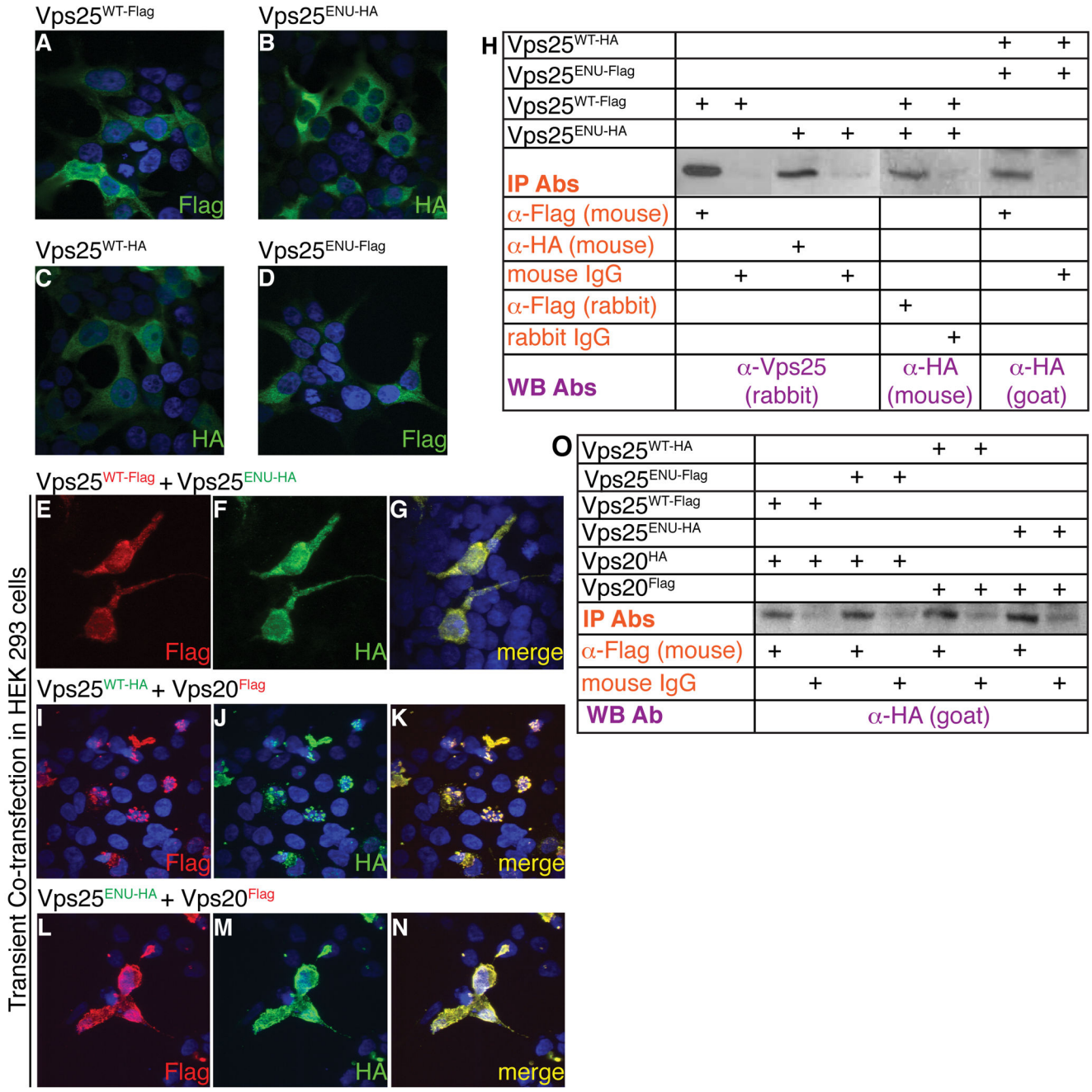

Figure 4. ESCRT-II/Vps25^{WT} and ESCRT-II/Vps25^{ENU} immunoprecipitate with ESCRT-III/Vps20 protein; the WT protein complex is mostly detected within puncta, while the mutant complex is diffuse throughout the cytoplasm

(A–G) Transient transfection of Vps25$^{WT\text{-}Flag}$, Vps25$^{WT\text{-}HA}$, Vps25$^{ENU\text{-}HA}$ or Vps25$^{ENU\text{-}Flag}$ alone or in combination, in HEK293 cells. IF with Flag or HA antibodies (Ab) reveals that Vps25^{WT} and Vps25^{ENU} mutant proteins co-localize within the cytoplasm, also within puncta.

(H) Co-immunoprecipitation (IP) of Vps25 WT and mutant proteins from cells transfected with $Vps25^{WT\text{-}Flag}$ and $Vps25^{ENU\text{-}HA}$ or with $Vps25^{WT\text{-}HA}$ and $Vps25^{ENU\text{-}Flag}$. IP with anti-Flag or anti-HA Ab; WB with anti-Vps25 or an anti-HA Ab.
(I–O) Both $Vps25^{WT\text{-}HA}$ and $Vps25^{ENU\text{-}HA}$ co-localize and co-immunoprecipitate with $Vps20^{Flag}$ in transfected HEK293 cells. However, subcellular localization of the mutant $Vps25^{ENU}$-Vps20 complex is diffuse throughout the cytoplasm, unlike the WT complex, which localizes to puncta. Abs used for IP and WB labeled orange and purple, respectively. See also Figure S4.

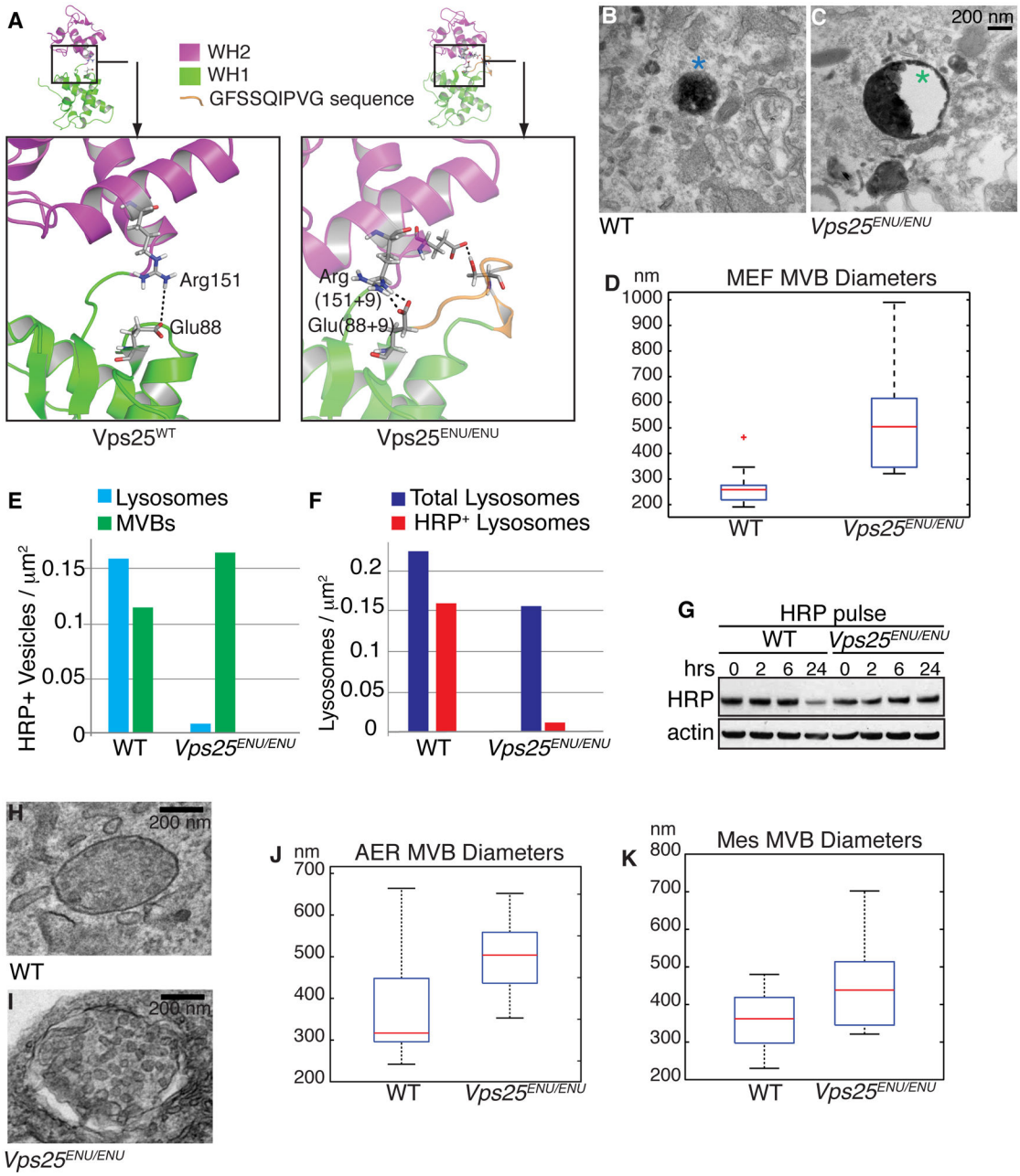

Figure 5. *Vps25* ENU-induced mutation yields low-levels of both WT and structurally altered mutant protein and is associated with engorged MVBs in cultured cells and limb AER and mesenchyme *in vivo*, resulting in perturbed endosomal trafficking

(A) Structural representation of WT and Vps25^{ENU} proteins reveals a conserved Glu88-Arg151 hydrogen bond between WH1 (green) and WH2 (magenta) domains. In the Vps25^{ENU} protein a new strong hydrogen bond (<2Å) Ser(IV)-Glu(105+9) is formed, due to the 9 amino acid insertion (orange). See also Figure S5.

(B–D) Transmission Electron Microscopy (TEM) reveals a significant increase in the diameters of multivesicular bodies (MVB) in E13.5 mutant *versus* WT MEFs treated with HRP. The box-and-whisker plot (D) depicts MVB diameters (in nanometers, nm) on the Y

axis and WT and mutant (*Vps25*$^{ENU/ENU}$) MVB sample populations on the X axis. Blue boxes represent the middle 50% of the values of the sample range; red lines represent the value of the median sample; legs and bars represent upper and lower limits of the diameter sample. Red cross indicates an outlier. Diameters measured in 16 WT and 12 mutant MVBs (***$p<0.0001$).

(E) 100 MVBs and 100 lysosomes counted in HRP-treated WT and mutant MEFs. In WT MEFs, HRP-positive MVBs (green) and lysosomes (blue) are present in approximately equal numbers, while in *Vps25*$^{ENU/ENU}$ MEFs HRP-positive lysosomes are negligible.

(F) Numbers of total (purple) and HRP-positive (red) lysosomes (100) counted and reported per surface areas (mm^2) in both WT and *Vps25*$^{ENU/ENU}$ MEFs, showing that in mutant MEFs HRP is not escorted to the lysosomes.

(G) WB analysis of MEFs treated with a 30 min HRP pulse, and chased for different times (hours, hrs), demonstrates abnormal HRP degradation in mutant MEFs.

(H–K) TEM reveals a significant increase in MVB diameters within the limb AER and mesenchyme compartments of E11.5 *Vps25*$^{ENU/ENU}$ (N=5) *versus* WT (N=2) embryos. The box-and-whisker plots (J,K), as detailed above (in D), depict MVB diameters (in nanometers, nm) on the Y axis and WT and *Vps25*$^{ENU/ENU}$ MVB sample populations on the X axis. Diameters measured in 13 WT and 12 mutant MVBs, in limb AER (*$p<0.05$). In limb mesenchyme diameters measured in 15 WT and 21 mutant MVBs (*$p<0.05$).

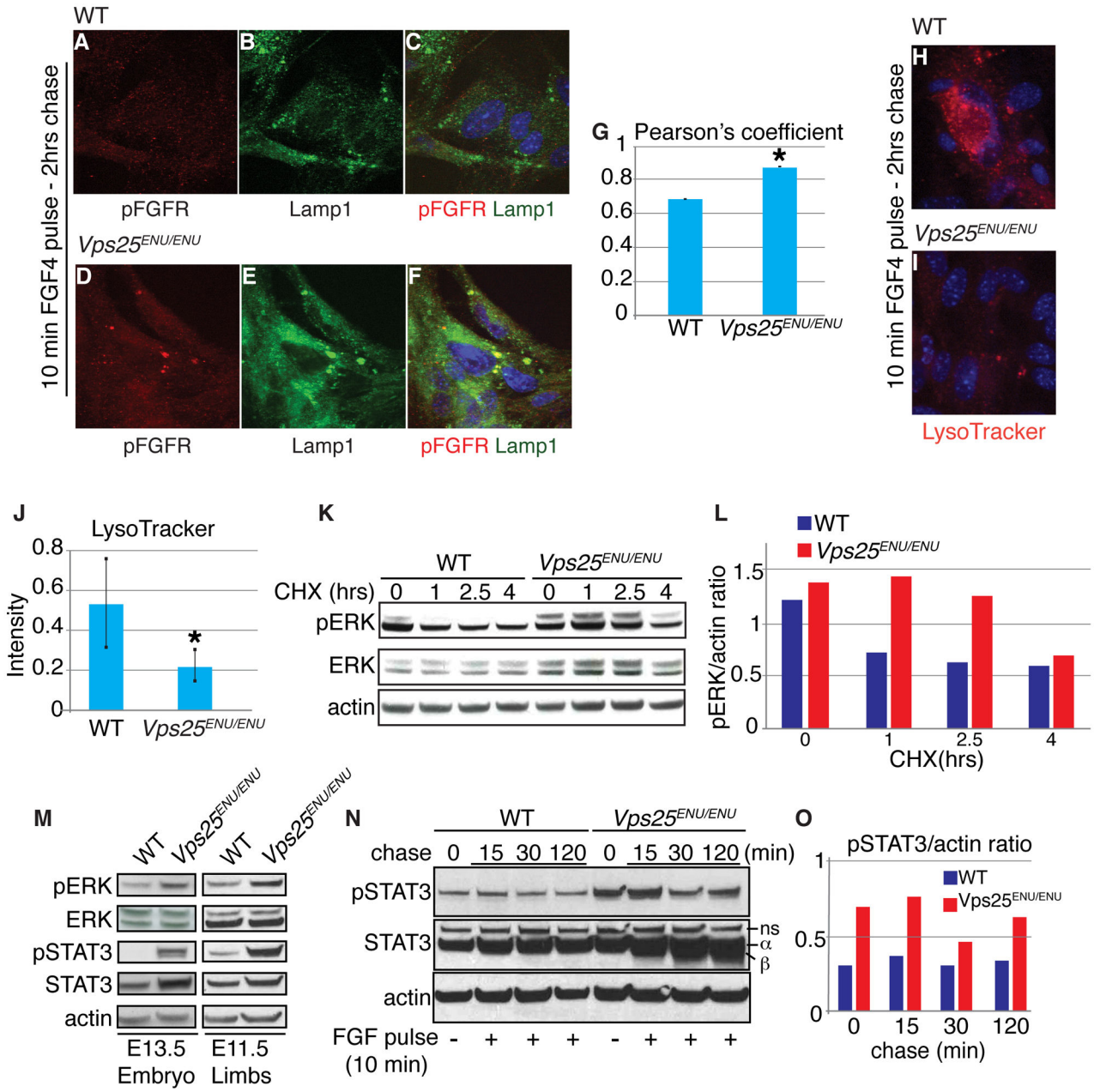

Figure 6. Vps25 ENU-induced mutation results in FGF receptor degradation defects and enhancement of FGF signaling in both cultured cells and limb buds *in vivo*

(A–G) IF for phospho(p)-FGFR following FGF4 pulse-chase in MEFs shows increased co-localization of pFGFR and Lamp1 in late endosomes (or MVBs) of mutant MEFs *versus* WT, quantified by Pearson's coefficient (*p < 0.05), indicating MVB sequestration of pFGFR.

(H–J) After a 10 min FGF4 pulse, WT and *Vps25*$^{ENU/ENU}$ MEFs were chased for 2 hours (hrs) and vesicular pH measured by LysoTracker staining. Quantification of signal intensity reveals significantly lower levels of staining in *Vps25*$^{ENU/ENU}$ MEFs, indicating lysosomal functionality defects (*p < 0.05).

(K,L) Assessment of pERK protein stability in WT and *Vps25*$^{ENU/ENU}$ MEFs treated with cycloheximide (CHX) for different times, indicated in hours, demonstrates abnormal protein degradation in mutant cells. ERK and actin as controls. Quantification of pERK levels over actin by ImageJ64 in WT (purple) and *Vps25*$^{ENU/ENU}$ (red) MEFs (L).
(M–O) WB of whole embryos (E13.5) and limbs (E11.5), as well as FGF4 pulse-chase experiment in MEFs, show increase of FGF second messengers and decreased pSTAT3 degradation, quantified by ImageJ64, in *Vps25*$^{ENU/ENU}$ (red) *versus* WT (purple) MEFs. Actin as control. min, minutes; ns, non-specific band.

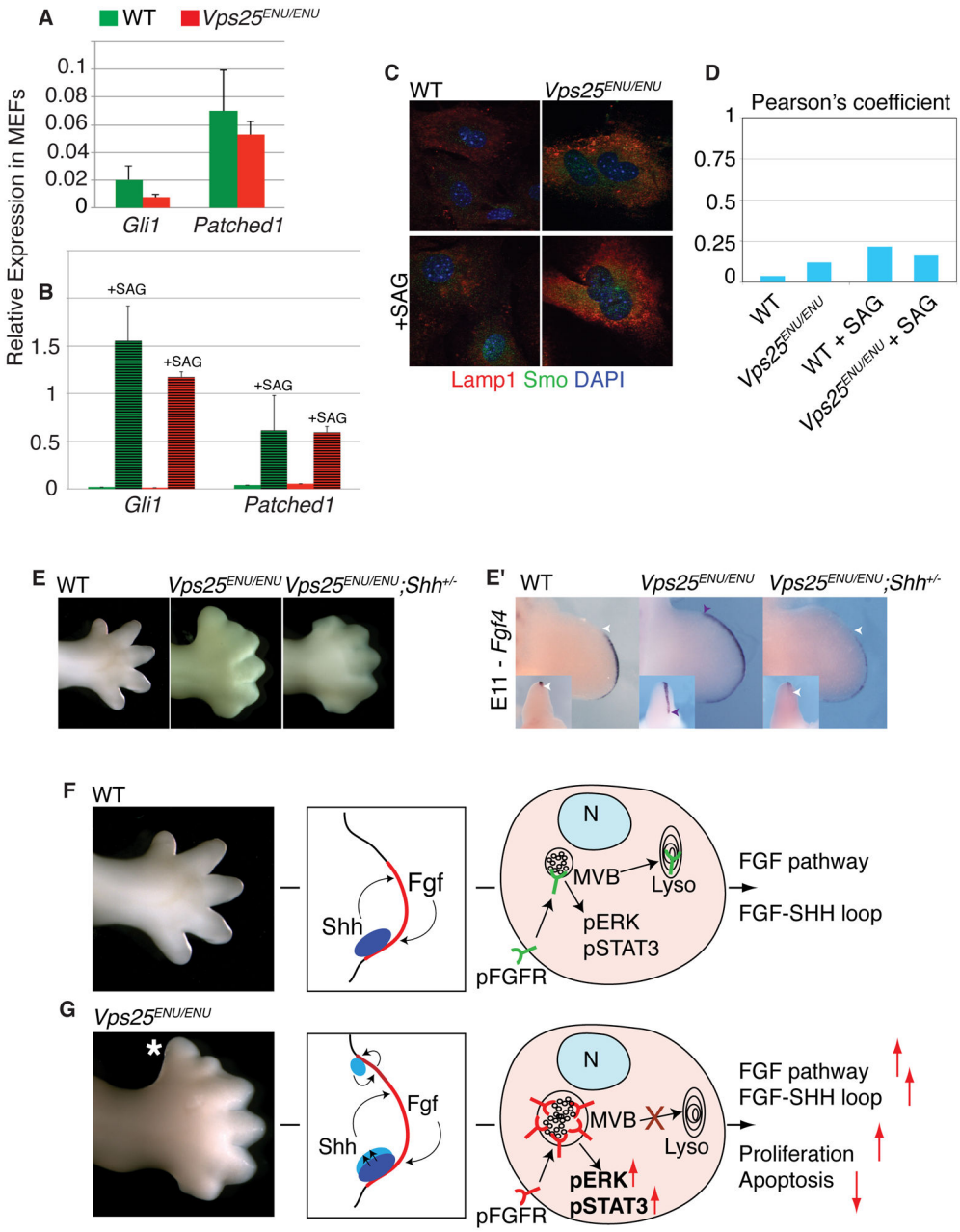

Figure 7. Vps25 ENU-induced mutation does not cause intrinsic enhancement of SHH signaling in cultured cells, whereas in *Vps25*$^{ENU/ENU}$ embryos polydactyly is partially rescued by limiting the FGF-SHH feedback loop

(A,B) qRT-PCR of *Gli1* and *Patched1* in WT (green) and *Vps25*$^{ENU/ENU}$ (red) MEFs, with (dashed bar) and without (solid bar) SAG treatment, demonstrates lack of statistically significant changes of both transcripts in WT *versus* mutant MEFs. (A) Independent MEF populations derived from 3 WT and 3 *Vps25*$^{ENU/ENU}$ embryos analyzed for biological replicates. (B) Independent MEF populations derived from 1 WT and 1 *Vps25*$^{ENU/ENU}$ embryo analyzed in technical triplicates.

(C,D) IF for Smoothened (Smo) (green) and Lamp1 (red) shows no accumulation of Smo in the engorged late endosomes of mutant MEFs, untreated or stimulated with SAG. Pearson's coefficient analysis of Smo trafficking confirms lack of co-localization of Smo and engorged Lamp1-positive endosomes in *Vps25*$^{ENU/ENU}$ MEFs untreated or stimulated with SAG (D). Engorged Lamp1-positive endosomes identified based on a mask selecting for pixels that are among the top 55% in Lamp1 signal intensity.

(E, E′) Partial rescue of digit number and reduction of anterior AER *Fgf4* expansion in *Vps25*$^{ENU/ENU}$*;Shh*$^{+/-}$ mutant HL buds. Normal *Fgf4* expression domain; white arrowheads. *Fgf4* spatial expansion; purple arrowheads.

(F,G) ESCRT-II/Vps25 constrains digit number during development by endosome-mediated selective modulation of the FGF-SHH signaling loop. Substantial loss of Vps25 WT and concomitant presence of Vps25 mutant protein, resulting from the ENU-induced mutation, lead to abnormal accumulation of pFGFR within engorged MBVs and perturbed trafficking to the lysosomes, producing increased levels of FGF second messengers. This triggers hyper-activation of FGF signaling that enhances the FGF-SHH feedback loop, yielding increased proliferation and decreased apoptosis in the limb bud. Overall, this causes polydactyly. See also Figure S7.